The Astrophysical Journal Letters, 956:L26 (6pp), 2023 October 10 https://doi.org/10.3847/2041-8213/acfd1d

A Single Ejection Model of the DART/Dimorphos Debris Trail

Yoonyoung Kim and David Jewitt
Department of Earth, Planetary and Space Sciences, UCLA, Los Angeles, CA 90095-1567, USA; yoonyoung@epss.ucla.edu
Received 2023 September 11; revised 2023 September 22; accepted 2023 September 25; published 2023 October 12

Abstract

The collision of the NASA DART spacecraft with asteroid Dimorphos resulted in the formation of a distinctive and long-lived debris trail, formed by the action of solar radiation pressure on ejected particles. This trail briefly displayed a double appearance, which has been interpreted as the result of a double ejection. We present a model that can produce a transient double trail without the need to assume a double ejection. Our model explains the appearance of the double trail as a projection of the cone walls when viewed from a large angle to the cone axis and avoids the problem of producing dust in two epochs from a single, instantaneous impact. The particles follow a broken power-law size distribution, with differential indices $q = 2.7 \pm 0.2$ ($1\ \mu\mathrm{m} \leqslant a \leqslant 2$ mm), 3.9 ± 0.1 ($2\ \mathrm{mm} < a \leqslant 1$ cm), and 4.2 ± 0.2 ($1\ \mathrm{cm} < a \leqslant 20$ cm). We find that the total trail mass in particles from 1 μm to 20 cm in size (for an assumed density 3500 kg m^{-3}) is $\sim 1.7 \times 10^7$ kg, rising to 2.2×10^7 kg, when extended to boulders up to 3.5 m in radius. This corresponds to 0.4%–0.6% of the mass of Dimorphos.

Unified Astronomy Thesaurus concepts: Asteroids (72); Impact phenomena (779); Near-Earth objects (1092)

1. Introduction

The UT 2022 September 26 collision of the NASA DART spacecraft with asteroid Dimorphos resulted in the formation of a long-lived debris trail, formed by the action of solar radiation pressure on solid particles ejected by the impact. This trail briefly appeared double but merged into a single trail within 2 weeks of the impact (Li et al. 2023; Opitom et al. 2023). The double trail was interpreted by Li et al. (2023) as evidence for a second discrete ejection event occurring ~5–7 days after the spacecraft impact. Moreno et al. (2023) considered a second ejection ~5.5 days after impact (see also Lin et al. 2023). These authors speculate that a second dust release might be caused by the delayed impact of debris from Dimorphos on the nearby asteroid Didymos or perhaps by complicated dynamical interactions within the Didymos/Dimorphos binary system. However, it is not obvious why these processes would be lagged from the main impact by nearly a week, given the high speed of ejecta from the impact and the small size of the Didymos/Dimorphos binary system (separation ~1.2 km).

In this Letter, we present an alternate model in which the appearance of the trail is accurately reproduced while the assumption of double ejection is not needed. Instead, the temporary double trail appearance is explained as the result of projection from the walls of a conical ejecta curtain, as is commonly observed in laboratory impact experiments (e.g., Melosh 1989). This projection effect fades with the rapidly changing observing geometry (including a threefold increase in the geocentric distance and a corresponding loss of spatial resolution) and as the trail progressively spreads, leading to a single trail morphology as observed at later times. We use our model in conjunction with Hubble Space Telescope (HST) data (Table 1) to estimate the particle size distribution and the total mass of material released by the DART/Dimorphos impact.

2. Model Description

The Dimorphos debris cloud exhibited three main structures: (1) an impact ejecta cone consisting of short-lived and irregular structures, (2) a diffuse envelope, and (3) a radiation pressure–swept debris trail with a temporarily double appearance (Li et al. 2023). In addition, dozens of impact-produced boulders up to ~7 m in diameter were detected in deep HST images (Jewitt et al. 2023). Our primary objective is to model the radiation pressure–swept trail.

To model the morphology of the debris trail, we used a Monte Carlo simulation of the dust (Ishiguro et al. 2007; Kim et al. 2017b). Previous applications of this model showed that projection from the walls of an impact cone can produce a double-tail morphology (Ishiguro et al. 2011; Kim et al. 2017a). Given the morphological similarity with the DART/Dimorphos trail, we consider a similar model. Specifically, we assume that the dust particles were impulsively launched in a conical ejecta curtain (see Melosh 1989) on UT 2022 September 26, 23:14:24.183 (Daly et al. 2023). We follow the motions of ejected particles in the curtain under the action of solar gravity and radiation pressure, following a procedure developed in Ishiguro et al. (2011). We consider the conical curtain to be symmetric with respect to a vector perpendicular to the asteroid surface (α_{cone}, δ_{cone}) with a half-opening angle of θ (i.e., the vertex angle of the cone is 2θ). The angular thickness of the cone walls is written $\delta\theta$. Particles are ejected uniformly in the angle range $\theta \pm (\delta\theta/2)$, with no particles outside this range.

The number of dust particles within a radius range from a to $a + da$ is given by a power-law distribution with size index q, $N(a)da = Na^{-q}da$, where N is the reference number of dust particles. We further represent the ejection terminal velocity as a power-law function of the particle radius, such that $v_\infty = V_0 a^{-k} v$. V_0 is the reference ejection velocity (m s^{-1}) of particles having $a = 1$ m, and k is the velocity power index. The dimensionless random variable $v \geqslant 0$ follows a Gaussian probability density function given by $P(v) = 1/(\sqrt{2\pi}\,\sigma_v)\exp(-(v-1)^2/2\sigma_v^2)$, where we set standard deviation $\sigma_v = 0.3$ (Ishiguro et al. 2013).

Table 1
Observations Used

UT Date and Time	ΔT_i[a]	r_H[b]	Δ[c]	α[d]	$\theta_{-\odot}$[e]	θ_{-V}[f]	$\delta_{\oplus}$[g]
2022 Sep 26 23:14 (Impact)	0.00	1.046	0.076	53.2	297.9	228.1	47.6
2022 Sep 27 07:25–07:44	0.35	1.045	0.075	53.7	297.3	227.7	47.7
2022 Sep 27 16:57–17:31	0.75	1.044	0.075	54.4	296.7	227.2	48.0
2022 Sep 28 02:28–03:02	1.14	1.043	0.074	54.9	296.0	226.6	48.1
2022 Oct 2 16:01–16:35	5.71	1.033	0.071	61.7	289.0	220.9	48.4
2022 Oct 5 18:38–19:12	8.82	1.027	0.071	66.0	285.4	217.6	46.7
2022 Oct 8 19:40–20:15	11.86	1.022	0.073	69.6	282.9	215.2	43.8
2022 Oct 11 20:42–21:16	14.90	1.018	0.075	72.5	281.5	213.6	40.1
2022 Dec 19 15:05–20:25	83.78	1.177	0.219	25.5	271.5	282.9	−3.8
2023 Feb 4 13:30–Feb 5 18:38	131.20	1.433	0.496	21.0	110.1	274.2	−6.1
2023 Apr 10 10:52–Apr 11 22:12	196.22	1.771	1.282	33.7	104.2	280.6	−2.1

Notes.
[a] Number of days from impact.
[b] Heliocentric distance, in astronomical units.
[c] Geocentric distance, in astronomical units.
[d] Phase angle, in degrees.
[e] Position angle of projected antisolar direction, in degrees.
[f] Position angle of negative heliocentric velocity vector, in degrees.
[g] Angle from orbital plane, in degrees.

The trajectories of the particles were computed from the terminal velocity and the ratio of radiation pressure acceleration to solar gravity, β. For spherical particles, β is approximately given by $\beta = 570/(\rho a_{\mu m})$, where ρ is the mass density of dust particles in kilogram per cubic meter and $a_{\mu m}$ is in microns (Burns et al. 1979). The density of the ejecta particles is not known, but for ease of comparison with the work of Moreno et al. (2023), we assumed $\rho = 3500\,\mathrm{kg\,m^{-3}}$. Because of the very small observer distance (0.076 au at the moment of impact), a small change in the observer position could have a significant effect on the morphology, so we used HST's precise position at a given time obtained from JPL Horizons. We performed multiple simulations with different parameter sets and then visually compared the resulting model images to the data to identify plausible parameters. The best-fit parameters are given in Table 2. Figure 1 compares the observations with the best-fit models.

Table 2
Input and Best-fit Parameters for the Dust Model

Parameter	Input Values	Best-fit Values
θ (deg)	40–90 with 5 intervals	60 ± 10
$\delta\theta$ (deg)	10–40 with 5 intervals	30 ± 10
α_{cone} (deg)	0–360 with 5 intervals	120–145
δ_{cone} (deg)	−90 to 90 with 5 intervals	10–25
V_0 ($\mathrm{m\,s^{-1}}$)	0.001–0.240 with 0.0005 intervals	0.0015 ± 0.0005
k	0.1–0.6 with 0.1 intervals	0.5 ± 0.1
q_1	2.5–4.5 with 0.1 intervals	2.7 ± 0.2 ($1\ \mu\mathrm{m} \leqslant a \leqslant 2$ mm)
q_2	2.5–4.5 with 0.1 intervals	3.9 ± 0.1 ($2\ \mathrm{mm} < a \leqslant 1$ cm)
q_3	2.5–4.5 with 0.1 intervals	4.2 ± 0.2 ($1\ \mathrm{cm} < a \leqslant 20$ cm)

3. Discussion

3.1. Morphology

The parameter ranges to be explored were selected based on previous studies of active comets and asteroid dust trails (Ishiguro et al. 2007; Kim et al. 2017a; Agarwal et al. 2023). Moreno et al. (2023) employed a piecewise model of Dimorphos in which the dust particles were ejected in two different velocity ranges (fast and slow), the latter in two epochs in order to generate two trails. Fast particles have $V \gg V_e$, where $V_e \sim 0.24\,\mathrm{m\,s^{-1}}$ is the system escape speed, while slow particles have $V \lesssim V_e$. They also employed a power-law representation of the particle size distribution and required two different power laws with a break at $a \sim 3$ mm in order to fit the data. Here, we ignore the high-velocity components associated with the earliest observations of the impact debris and model only the trail particles, which are ejected slowly enough that radiation pressure dominates their motion. Specifically, we ignore particles with ejection speeds $V \gg V_e$ because these particles do not contribute to the trail we seek to model.

We first used the cone axis solutions (141°, 25°) and (120°, 10°) from Li et al. (2023) to find the ejection terminal velocity and cone angle parameter sets, fitting the double trail position angle and trail width of the HST data. We assume that the cone is symmetric about its long axis; the real cone may include asymmetries that alter the appearance slightly when projected into the plane of the sky. The double trail appearance was easily obtained assuming low ejection velocities. We derived $V_0 \sim 1.5\,\mathrm{mm\,s^{-1}}$ (for $a = 1$ m particles) and $k \sim 0.5$, indicating that the maximum speed was $\sim 1.5\,\mathrm{m\ s^{-1}}$ for $a = 1\ \mu$m particles. At $k < 0.5$, the wedge angle of the October 8 data could not be matched, and at $k > 0.5$, the trail in the December 19 data widened too steeply. High-velocity impact experiments show a weak and inverse relation between fragment speed and size, consistent with the small exponent derived here (Nakamura & Fujiwara 1991; Giblin 1998).

The smallest particle size (1 μm) was determined from the length of the trail in the earlier images. The largest particle size ($a \gtrsim 0.2$ m) was obtained from the absence of a clear gap between the nucleus and the trail in the latest images. Terminal velocity v_∞ is the excess speed after particles climbed out of the potential well of the system, and the actual ejection speed U is given by $U = \sqrt{v_\infty^2 + V_e^2}$, where V_e is the gravitational escape speed from the system. Over the size range

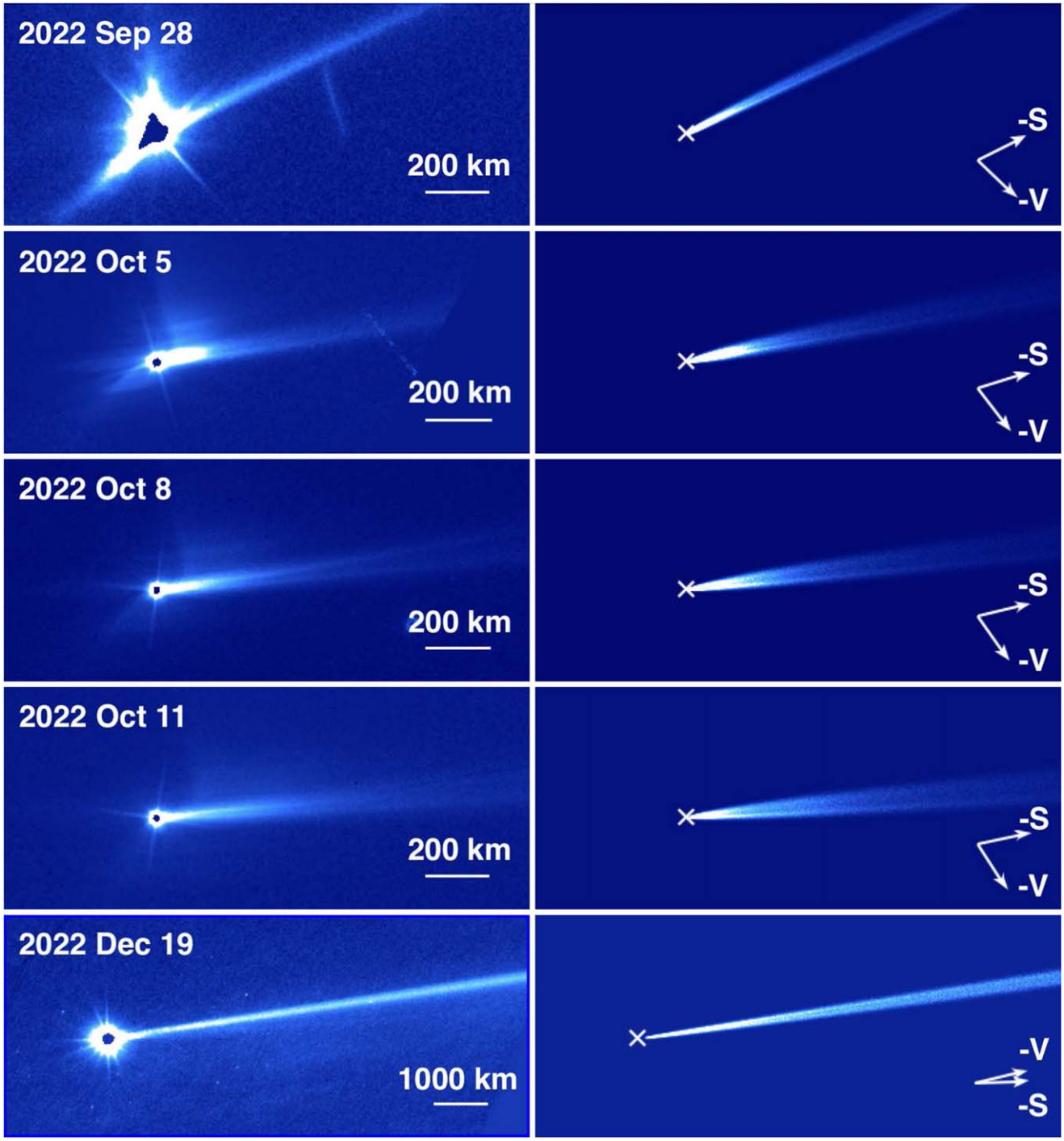

Figure 1. Comparison between HST images (left) and Monte Carlo models (right). A linear scale bar, the projected antisolar direction ($-S$), and the negative heliocentric velocity vector ($-V$) are indicated. The Dimorphos location is marked with a cross in each panel. Note the scale change in the last row of panels.

$1\ \mu\mathrm{m} < a < 0.2\ \mathrm{m}$, the ejection speed U varies from 0.24 to $1.5\ \mathrm{m\ s^{-1}}$.

Unless the cone axis deviates significantly from the solutions used in Li et al. (2023) and Cheng et al. (2023), no significant difference appears in the morphology. We find a best-fit half-opening angle of $\theta = 60^\circ \pm 10^\circ$ (in excellent agreement with $\theta = 62^\circ \pm 5^\circ$ from Li et al. 2023) with the cone axis at $120^\circ \lesssim \alpha_{\mathrm{cone}} \lesssim 145^\circ$ and $10^\circ \lesssim \delta_{\mathrm{cone}} \lesssim 25^\circ$. Assuming the cone axis at (141°, 25°), Figure 2 shows the angle between the trail axis and the line of sight, measured from the nucleus. Interestingly, the viewing angle reached 90° in early October when the double tail was first reported (Li et al. 2023; Murphy et al. 2023) and maintained a large angle during the period when the double tail was observed. The double trail was not noticed in the first week after impact presumably because the ejecta cone had not expanded enough for the walls to appear separated (see Figure 1).

As such, our model explains the temporary appearance of the double trail as a projection of the cone walls when viewed from a large angle to the cone axis. The double appearance faded after mid-October as the observing geometry changed rapidly (toward a larger observer distance, poorer spatial resolution,

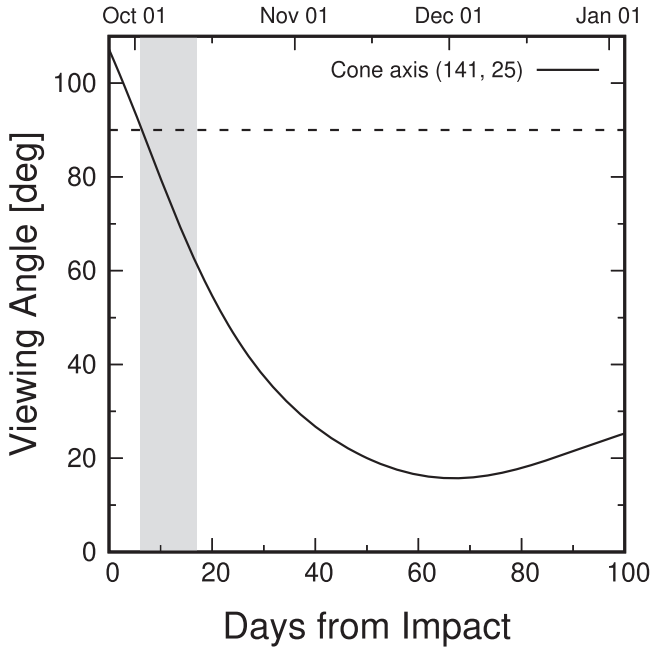

Figure 2. Viewing angle (angle between the trail axis and the line of sight) as a function of time, expressed as days after impact. The shaded region indicates when the double tail was observed. The ejecta cone is viewed edge-on when viewing angle = 90° (dashed line), at which point the walls of the hollow cone are most clearly visible.

and smaller cone-viewing angle) and the particles dispersed by radiation pressure progressively filled the cone. The latter takes about 70 days to fill the cone, after which a single trail morphology appears regardless of the viewing geometry.

3.2. Size Distribution and Mass

The particle size dependence of the radiation pressure parameter, β, imposes a size gradient along the length of the trail, from large particles near the impact site to small ones far away. Combined with measurements of the trail surface brightness as a function of position, this size gradient can be used to determine the particle size distribution in the ejected material. For reference, Figure 3 shows an HST image taken on UT 2023 February 4 annotated to show the approximate distances along the trail to which particles of a given size have been swept by radiation pressure in the ∼4 months since impact. Evidently, particles smaller than $a \sim 1$ mm have already been removed from the HST field of view by this date under the action of solar radiation pressure.

We used HST observations (Table 1) in order to determine the surface brightness of the trail. The nucleus and surroundings were saturated in most early HST images and, consequently, we did not measure or fit within a few arcseconds of the nucleus. As noted by Li et al. (2023) and Moreno et al. (2023), no single power law can fit the surface brightness measurements. In agreement with this conclusion, our models yield $q = 2.7 \pm 0.2$ for $1\ \mu\text{m} \leqslant a \leqslant 2$ mm and $q = 3.9 \pm 0.1$ for $2\ \text{mm} < a \leqslant 1$ cm.

In addition, the surface brightness profile close to the nucleus allows us to place a constraint on particles even larger than 1 cm. We find that models with $q < 4.0$ leave too many large particles within ∼5″ to 12″ of the nucleus, where the data show a surface brightness downturn (Figure 4). Conversely, power laws with $q \gtrsim 4.4$ are inconsistent with the data by underpredicting the near-nucleus surface brightness, leaving $q = 4.2 \pm 0.2$ as our best estimate of the large particle index. We conclude that particles larger than ∼1 cm are distributed according to a steeper power law than smaller particles.

In summary, the best-fit size distribution obtained from our models is

$$N(a)da = \begin{cases} N_1\, a^{-(2.7\pm0.2)}\, da & \text{for } 1\times10^{-6} \leqslant a \leqslant 2\times10^{-3} \\ N_2\, a^{-(3.9\pm0.1)}\, da & \text{for } 2\times10^{-3} < a \leqslant 1\times10^{-2}, \\ N_3\, a^{-(4.2\pm0.2)}\, da & \text{for } 1\times10^{-2} < a \leqslant 2\times10^{-1} \end{cases} \quad (1)$$

where a is expressed in meters, and N_1, N_2, and N_3 represent the reference dust production rates.

For comparison, Li et al. (2023) found a break in the size distribution for particle radii of a few millimeters, with $q = 2.7 \pm 0.2$ for smaller dust and $q = 3.7 \pm 0.2$ for larger particles. Moreno et al. (2023) fitted a broken power law with $q = 2.5$ for particles $a \lesssim 3$ mm and with a higher slope of $q = 3.7$ for particles $a \gtrsim 3$ mm. These results are concordant with those in Equation (1). Broken power-law size distributions have also been reported in the debris from natural asteroid breakups (Jewitt et al. 2019, 2021; Ye et al. 2019).

The important feature of Equation (1) is that it shows that the size distribution steepens toward larger particle sizes. We note that the choice of the largest particle size ($a_{\max}$) does not have a significant effect on the near-nucleus surface brightness, indicating that $a_{\max}$ could be much larger than 0.2 m, even extending to the size of the boulders ($a_{\max} \lesssim 3.5$ m; Jewitt et al. 2023).

For a collection of spheres, the total cross section, C_d, is given by

$$C_d = \int_{a_{\min}}^{a_{\max}} \pi a^2 N(a)\, da, \quad (2)$$

where we derive the reference number N_1, N_2, and N_3 from the early photometric result by substituting $N(a)da$ in Equation (1). The total mass can be estimated from the early photometry (i.e., brightening) combined with the carefully determined size distribution. Graykowski et al. (2023) reported brightening on impact ($\Delta C \sim 3.82\ \text{km}^2$ increase in cross-sectional area from the peak to the nucleus level and $\Delta C \sim 1.64\ \text{km}^2$ after the fast-moving ejecta moved out of the photometric aperture). Substituting $\Delta C = 1.64\ \text{km}^2$ gives $N_2 = 480$, where $N_1 = N_2 \times 0.002^{(2.7-3.9)}$ and $N_3 = N_2 \times 0.01^{(4.2-3.9)}$.

The total mass of the dust cloud, M_d, is given by

$$M_{\rm d} = \int_{a_{\min}}^{a_{\max}} \frac{4}{3}\pi\rho_d a^3 N(a)\, da, \quad (3)$$

where we find that the total mass of the trail in the particle size range from 1 μm to 0.2 m in size is $\sim 1.7 \times 10^7$ kg (assumed density 3500 kg m^{-3}), corresponding to about 0.4% of the mass of Dimorphos. Extending this size distribution to the largest observed boulder radius 3.5 m (Jewitt et al. 2023), the total escaping ejecta mass from the DART spacecraft impact is estimated to be at least 2.2×10^7 kg, equal to about 0.6% of the mass of Dimorphos. This value is compared to the total boulder mass $M_b = 8 \times 10^6$ kg (scaled to $\rho = 3500$ kg m^{-3}; Jewitt et al. 2023). We note that the observed boulders reported in Jewitt et al. (2023) are not part of the radiation pressure–dominated

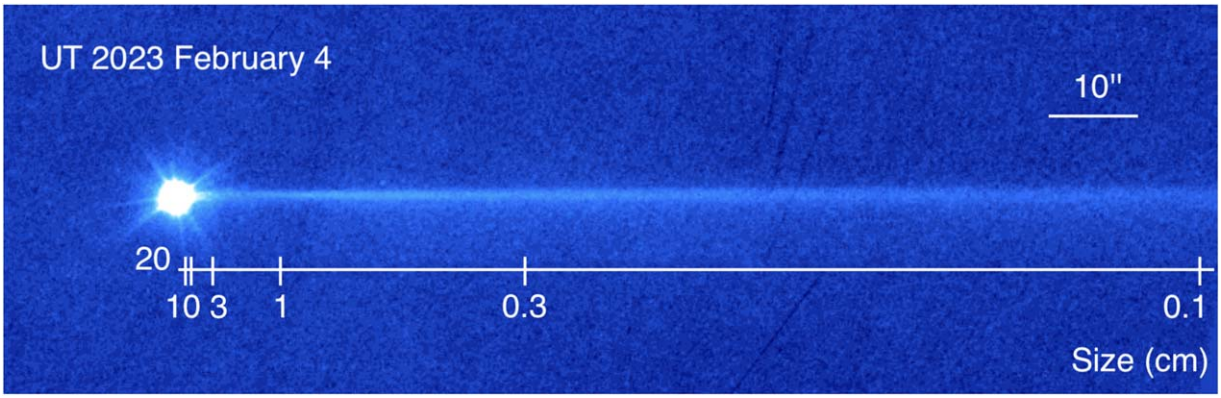

Figure 3. Composite HST image from UT 2023 February 4, rotated so that the trail lies horizontally. We mark the distances reached by dust particles under the action of radiation pressure, as a function of their radius (in centimeters).

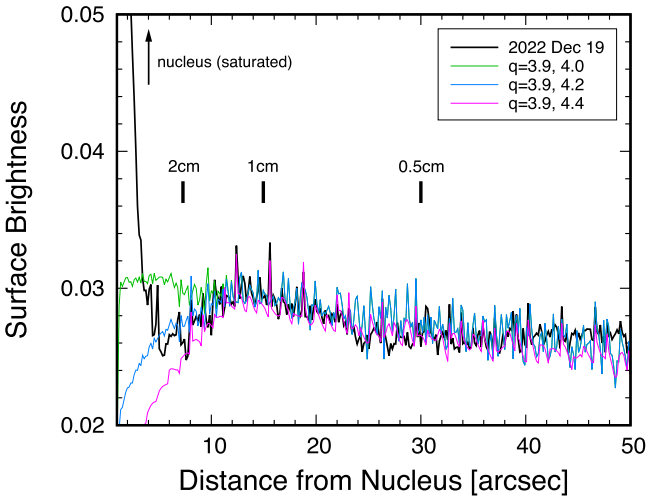

Figure 4. The surface brightness vs. distance along the trail (black line; $0.001 = 27.2$ mag arcsec^{-2}). Lines show models for a power law, broken at $a = 1$ cm, with differential indices $q = 3.9$ and 4.0 (green), $q = 3.9$ and 4.2 (blue), and $q = 3.9$ and 4.4 (magenta). Approximate locations of particles as a function of their radius are marked. The nucleus was saturated in the data and was not fitted.

trail, and there may be uncertainty in the actual boulder size and fallback mass.

We calculate the fallback mass of large dust particles within a size range of $a_{\rm max}$ (largest trail particle observed) and $a_{\rm b}$ (largest boulder observed),

$$M_{\rm fb} = \int_{a_{\rm max}}^{a_{\rm b}} \frac{4}{3}\pi\rho_d a^3 N(a)\,da, \qquad (4)$$

where we set $a_{\rm max} = 0.2$ m and $a_{\rm b} = 3.5$ m to find $M_{\rm fb} \sim 5.4 \times 10^6$ kg. This fallback material is enough to coat the entire surface of Dimorphos to a depth of $D = M_{\rm fb}/(4\pi r_n^2 \rho) \sim 2$ cm and could be contained within a hemispherical cavity ~15 m in radius. All of the above mass estimates are subject to potentially considerable (factor of 2 or larger) systematic uncertainties since they rely upon unmeasured particle densities, albedos, and phase function.

One difference between the present study and those of Li et al. (2023) and Moreno et al. (2023) is our use of data from a larger range of dates. We model HST imaging obtained up to 2023 April 10 (i.e., 7 months from impact) whereas Li et al. (2023) used HST data taken up to 2022 October 14 (3 weeks from impact) and Moreno et al. (2023) modeled the same HST data supplemented by ground-based images extending to 2022 December 24 (i.e., 3 months from impact). The later observations (Table 1) allow more time for the largest, slowest particles to move away from Dimorphos. They provide the best evidence for the lack of a clear gap near the impact site and so for the existence of a second break in the size distribution.

A second difference is that our model does not require the assumption of a delayed ejection of unclear origin, occurring nearly a week after the DART impact. Photometry places an independent constraint on secondary dust ejection because a separate mass-loss event should cause a delayed trail brightening in proportion to the added cross section. For example, Moreno et al. (2023) infer that the masses of the primary and secondary trails are in the ratio 4.3:3.0 (see their Table 4). With similar size distributions in the two trails, this would also be the ratio of the cross sections. The emergence of the secondary trail should then increase the total trail brightness by $3/4.3 \sim 70\%$ starting 5–7 days after the impact.

Figure 5 shows the scattering cross section of the debris trail within 50 km of Dimorphos. We used the aperture photometry from Extended Data Figure 4(B) of Li et al. (2023), from which the contribution to the photometry from Didymos/Dimorphos has been subtracted. We assumed a geometric albedo 0.1 (for easy comparison with Moreno et al. 2023)[1] and a phase function of 0.04 magnitudes degree^{-1} in order to calculate the cross section from the photometry. We also show an exponential function, $C = C_0 \exp(-t/T)$, least-squares-fitted to the data. The fit matches the data well given initial cross section $C_0 = 2.2$ km^2 and e-folding decay time $T = 5.27 \pm 0.01$ days. The cross section shows no evidence for an increase at the nominal time of the second ejection (impact +5 to 7 days, marked in the figure by a short horizontal bar). Instead, the cross section is larger than the fitted value only at $t = 8.8$ days but returns to the exponential decay by $t = 11.8$ days. Independent ground-based data provide no support for a brightening at 8.8 days (Graykowski et al. 2023 and Moreno et al. 2023) but are subject to larger uncertainties than the HST measurements. We conclude that published evidence for a post-impact trail brightening is limited to a single HST measurement from $t = 8.8$ days and that, while the

[1] Naidu et al. (2020) measured albedo 0.15 ± 0.04. We examined NEOWISE data in search of thermal emission from the system, finding images at 3.4 and 4.6 μm. However, the NEOWISE signal-to-noise ratio is insufficient to accurately estimate the albedo.

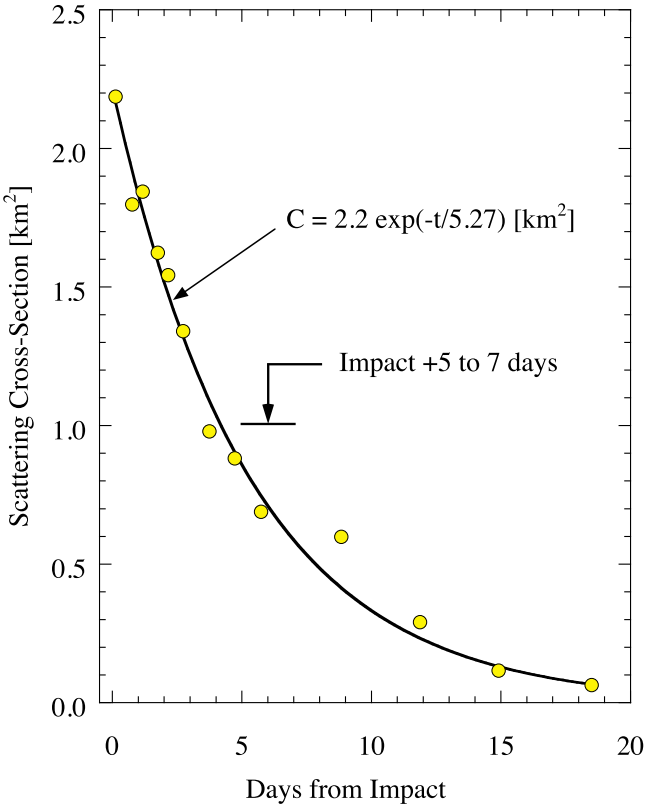

Figure 5. Scattering cross section of the debris trail within a 50 km radius projected aperture as a function of time. The solid black line shows an exponential fit to the data. The secondary tail ejection time from the model of Li et al. (2023) is indicated.

available photometric data do not absolutely rule out the possibility of a delayed brightening of the trail, neither do they provide compelling evidence for it. More and better photometric data are required. We thus believe that our single ejection model is consistent with the available data.

We end with a reminder that Monte Carlo models are necessarily nonunique. In this sense, the broad agreement between the particle size distributions presented here and those by Li et al. (2023) and Moreno et al. (2023) is encouraging. The distinction of the current model is that it satisfies Occam's razor by not requiring the assumption of a second ejection of uncertain origin in order to produce the double trail.

4. Summary

We present a single ejection model for the DART-produced double debris trail of asteroid Dimorphos, with the following results:

1. The combined HST data set can be matched by a size distribution with three segments, with differential power-law indices $q_1 = 2.7 \pm 0.2$ ($1\ \mu\text{m} \leqslant a \leqslant 2$ mm), $q_2 = 3.9 \pm 0.1$ ($2\ \text{mm} < a \leqslant 1$ cm), and $q_3 = 4.2 \pm 0.2$ ($1\ \text{cm} < a \leqslant 20$ cm).
2. The ejected mass in particles up to 3.5 m in radius (i.e., the size of the largest ejected boulder) is 2.2×10^7 kg (assumed density 3500 kg m^{-3}), corresponding to about 0.6% of the mass of Dimorphos. Systematic uncertainties on the ejected particle mass are likely a factor of 2, or more, depending especially on the unmeasured values of the particle density, albedo, and phase function.
3. Our model explains the temporarily double appearance of the trail as a projection of the ejection cone walls when viewed from a large angle to the cone axis. A delayed ejection is not needed to explain the second trail.

Acknowledgments

We thank the anonymous referee for a prompt review and Jian-Yang Li for comments. Based on observations made with the NASA/ESA Hubble Space Telescope, obtained from the data archive at the Space Telescope Science Institute. STScI is operated by the Association of Universities for Research in Astronomy, Inc. under NASA contract NAS 5-26555. Support for this work was provided by NASA through grant Nos. GO-17289, GO-17293, and GO-17297 from the Space Telescope Science Institute, which is operated by auRA, Inc., under NASA contract NAS 5-26555.

Facility: HST.

ORCID iDs

Yoonyoung Kim https://orcid.org/0000-0002-4676-2196

References

Agarwal, J., Kim, Y., Kelley, M. S. P., et al. 2023, arXiv:2309.12759
Burns, J. A., Lamy, P. L., & Soter, S. 1979, Icar, 40, 1
Cheng, A. F., Agrusa, H. F., Barbee, B. W., et al. 2023, Natur, 616, 457
Daly, R. T., Ernst, C. M., Barnouin, O. S., et al. 2023, Natur, 616, 443
Giblin, I. 1998, P&SS, 46, 921
Graykowski, A., Lambert, R. A., Marchis, F., et al. 2023, Natur, 616, 461
Ishiguro, M., Hanayama, H., Hasegawa, S., et al. 2011, ApJL, 741, L24
Ishiguro, M., Kim, Y., Kim, J., et al. 2013, ApJ, 778, 19
Ishiguro, M., Sarugaku, Y., Ueno, M., et al. 2007, Icar, 189, 169
Jewitt, D., Kim, Y., Li, J., et al. 2023, ApJL, 952, L12
Jewitt, D., Kim, Y., Luu, J., et al. 2019, ApJL, 876, L19
Jewitt, D., Li, J., & Kim, Y. 2021, AJ, 162, 268
Kim, Y., Ishiguro, M., & Lee, M. G. 2017a, ApJL, 842, L23
Kim, Y., Ishiguro, M., Michikami, T., et al. 2017b, AJ, 153, 228
Li, J.-Y., Hirabayashi, M., Farnham, T. L., et al. 2023, Natur, 616, 452
Lin, Z.-Y., Vincent, J.-B., & Ip, W.-H. 2023, A&A, 676, A116
Melosh, H. J. 1989, Impact Cratering: A Geologic Process (Oxford: Oxford Univ. Press)
Moreno, F., Bagatin, A. C., Tancredi, G., et al. 2023, PSJ, 4, 138
Murphy, B. P., Opitom, C., Snodgrass, C., et al. 2023, in Asteroids, Comets, Meteors Conf. (Houston, TX: Lunar and Planetary Institute), 2152, https://www.hou.usra.edu/meetings/acm2023/pdf/2152.pdf
Naidu, S. P., Benner, L. A. M., Brozovic, M., et al. 2020, Icar, 348, 113777
Nakamura, A., & Fujiwara, A. 1991, Icar, 92, 132
Opitom, C., Murphy, B., Snodgrass, C., et al. 2023, A&A, 671, L11
Ye, Q., Kelley, M. S. P., Bodewits, D., et al. 2019, ApJL, 874, L16